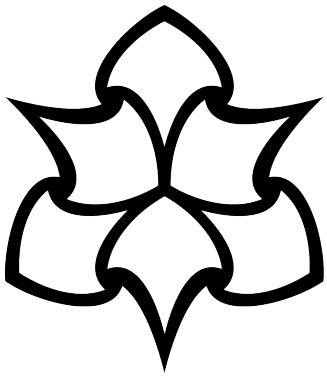

Numerical modelling of nonlinear extreme waves in presence of wind

NING Dezhi [1, 2], DU Jun [2, 4], BAI Wei [3], ZHANG Chongwei [2] *, TENG Bin [2]

1 State Key Laboratory of Hydrology-Water Resources and Hydraulic Engineering, Hohai University, Nanjing 210098, China

2 State Key Laboratory of Coastal and Offshore Engineering, Dalian University of Technology, Dalian 116023, China

3 School of Computing, Mathematics and Digital Technology, Manchester Metropolitan University, Chester Street, Manchester M1 5GD ,UK

4 China Communications Planning and Design Institute for Water Transportation LTD., Beijing 100007, China

Abstract

A numerical wave flume with fully nonlinear free surface boundary conditions is adopted to investigate the temporal characteristics of extreme waves in the presence of wind at various speeds. Incident wave trains are numerically generated by a piston-type wave maker, and the wind-excited pressure is introduced into dynamic boundary conditions using a pressure distribution over steep crests, as defined by Jeffreys' sheltering mechanism. A boundary value problem is solved by a higher-order boundary element method (HOBEM) and a mixed Eulerian-Lagrangian time marching scheme. The proposed model is validated through comparison with published experimental data from a focused wave group. The influence of wind on extreme wave properties, including maximum extreme wave crest, focal position shift, and spectrum evolution, is also studied. To consider the effects of the wind-driven currents on a wave evolution, the simulations assume a uniform current over varying water depth. The results show that wind causes weak increases in the extreme wave crest, and makes the nonlinear energy transfer non-reversible in the focusing and defocusing processes. The numerical results also provide a comparison to demonstrate the shifts at focal points, considering the combined effects of the winds and the wind-driven currents.

Key words: extreme waves, fully nonlinear numerical wave flume, higher-order boundary element, wave focusing, Jeffreys' sheltering mechanism

Foundation item: The National Natural Science Foundation of China under contract Nos. 51679036, 51490672 and 51709038; the UK-China Industry Academia Partnership Programme under contract No. UK-CIAPP\73; the Fundamental Research Funds for the Central Universities under contract Nos. DUT17GJ202 and DUT16RC(3)113; and the Open Foundation of State Key Laboratory of Hydrology-Water Resources and Hydraulic Engineering under contract No. 2016490111.
*Corresponding author, E-mail: chongweizhang@dlut.edu.cn

1 Introduction

Under actual ocean conditions, strong nonlinear extreme waves, which are identified by their exceptionally large height, steep shape, asymmetric wave form, and unpredictability, can pose a serious threat to ships and offshore structures. Currently, there is no consensus on a unique definition for extreme wave events. One definition that is often used is based on the height. A wave is considered to be extreme if its height satisfies the condition of being greater or equal to two point two times the size of the significant wave height (Kharif et al., 2008). Several mechanisms have been suggested as the possible causes for the extreme waves. The first mechanism is high-order nonlinearity (higher than the third order), causing extreme waves to occur in the deep water. The nonlinear interactions can transfer energy among the Fourier modes and excite chaotic mode evolutions, which can generate a single extremely large wave with an outstanding crest height, such as a rogue wave (Mori et al., 2002). The second mechanism is modulation, or Benjamin–Feir instability (Benjamin and Feir, 1967), for the extreme waves formed by a narrow-band and deep-water wave train. This mechanism has been investigated extensively both analytically and numerically (Osborne et al., 2000; Onorato et al., 2001; Onorato et al., 2002). Additionally, dispersive spatial-temporal focusing has been verified to effectively induce the extreme waves through the superposition of different frequency wave components at a specific time and position (Kharif et al., 2001). The third possible mechanism for the extreme wave generation may lie in the energy focusing in a small spatial area during a short time, thus generating an abnormally large wave (Johannessen and Swan, 2001; Brandini and Grilli, 2001; Fuhrman and Madsen, 2006). Overall, these studies provided a good understanding of the mechanisms of extreme wave formation.

On the basis of the above mechanisms, numerous experiments and numerical investigations have been conducted regarding the physical characteristics of the extreme waves. Longuet-Higgins (1952) was one of the earliest pioneers to investigate the statistics of the extreme waves, who then clarified the effects of finite bandwidth and nonlinearity (Longuet-Higgins, 1980). Baldock et al. (1996) created wave focusing events using many superimposed regular wave trains based on a linear wave theory, and examined the effects of nonlinear wave–wave interactions on structure in uni-directional wave groups. They subsequently introduced the concept of a group inversion in an

experimental context to investigate the free surface profile of focused wave groups. The directional focused wave group was studied experimentally by Johannessen and Swan (2001), who conclude that the directionality of the wave field has a profound effect on the nonlinearity of a large wave event, and that large directionally spread waves are much less nonlinear than the unidirectional waves.

Grue et al. (2003) studied the kinematics of the focused waves in the deep water and found that Stokes drift and a corresponding return flow beneath a focused wave group were inherent in all extreme wave events. In terms of the numerical simulation, Ducrozet et al. (2008) developed an efficient fully nonlinear potential flow model based on a high-order spectral (HOS) method to simulate the propagation of 3-D directional wave fields. Two methods, meshless local Petrov-Galerkin method (MLPG_R) and quasi-arbitrary Lagrangian-Eulerian finite element method (QALE-FEM), were also developed and compared by Ma (2007). Hu and Zhang (2014) used a Morlet wavelet spectrum method to analyze numerical and field measurement data on the extreme wave process. On the basis of a comparison of energy characteristics, it was found that rogue wave generation depended not only on the continuous transfer of the wave train energy to a certain region where its maximum energy finally occurs, but also on the distinct shift of the converged energy to high-frequency components in a very short time. Nevertheless, none of these studies considered the direct effects of wind on extreme wave events.

The extreme waves generally do not exist in isolation, and are commonly observed as being accompanied by wind (Mori and Yasuda, 2002). In the process of a wave propagation, the wind energy is transferred to the wave group, which has a strong influence on the wave propagation and the nonlinear characteristics. Therefore, it is critical to study the influence of wind on the propagation of extreme waves and their nonlinear characteristics. Liu et al. (2004) conducted an exploratory observational study of the generation and propagation of the extreme, rogue waves in the southern Indian Ocean, based on wave measurements. Touboul (2007) performed the numerical simulations of the extreme wave evolution in wind using a high-order spectral method based on Jeffreys' sheltering mechanism and modulation instability.

In addition, some numerical simulations have been established by solving the Navier-Stokes equations, as in Sullivan et al. (2000), Sullivan et al. (2004), Sullivan and McWilliams (2002), Fulgosi et al. (2003) and Nakayama and Sakio (2002). Kharif et al. (2008) and Touboul et al. (2006)

introduced an additional air pressure at the free surface boundary conditions by considering Jeffreys' sheltering mechanism. Yan and Ma (2011) presented an improved model for evaluating the effects of the air pressure on 2-D extreme waves by analyzing the pressure distribution over the extreme waves using the QALE-FEM and StarCD approaches. The effects of wind on two-dimensional dispersive focusing wave groups were also studied by Tian and Choi (2013). The direct comparisons of measurements and simulations were made by including wind-driven currents in the simulations. Zou and Chen (2016) investigated the effects of wind on the evolution of the 2-D dispersive focusing wave groups using a two-phase flow model.

Comprehensive numerical study of the evolution of nonlinear extreme waves under wind forcing is by no means complete, however, and new understandings of this phenomenon are still required for the purpose of aiding engineering designs in harsher environments. In the present study, the effects of some important parameters, such as wind speed, input wave amplitude, and spectrum bandwidth on the formation of extreme waves and their corresponding temporal–spatial–spectral evolution are further evaluated. In addition to this, the combined effect of wind and wind-driven currents are compared to address focal point shifts. In this paper, a detailed description of the numerical model is presented in Section 2. A higher-order boundary element method (HOBEM) based on the potential-flow theory was adopted in this study. Compared with the methods described above that rely on solving the Navier-Stokes equations the present numerical model has clear advantages with respect to computation efficiency. Additionally, regarding the simulation of free surface waves, the present method has fewer numerical dissipations than those based on the Navier-Stokes equations for long time simulation. The proposed numerical model is further validated by comparison with published experimental data in Section 3, and the numerical results are discussed in Section 4. Finally, conclusions are provided in Section 5.

2 Numerical model

The interactions between the extreme waves and wind with velocity u in a two-dimensional (2-D) fluid domain are described in Fig. 1. The free surface, wave maker, seabed and tank end are denoted by Γ_f, Γ_i, Γ_d, and Γ_r, respectively. A Cartesian coordinate system, Oxz, was used so that the origin is located over the still water level at the left end of the domain, and the z-axis is positive in

the upward direction. It was assumed that the fluid is incompressible, inviscid, and the flow motion irrotational so that a velocity potential exists in the fluid domain. Considering that there are currents induced by wind and assuming the currents are uniformly distributed along the water depth, the total velocity potential in the fluid domain can then be expressed as $\Phi = u_0 x + \phi(x, z, t)$, where u_0 is the steady uniform current velocity and $\phi(x, z, t)$ is the perturbation potential. In this study, the magnitude of the uniform current was empirically defined as 0.9% of the free-stream wind speed u, i.e., u_0=0.9%u, the same value used by Tian and Choi (2013) and Zou and Chen (2016). Both the total velocity potential and perturbation potential satisfy the Laplace equation in the computational domain Ω.

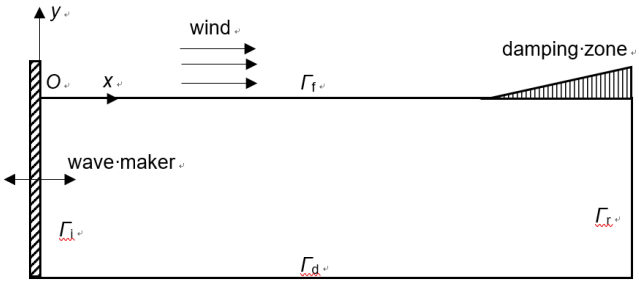

Fig.1. Sketch of the numerical wave flume

Given the boundary conditions, the velocity potential ϕ can be determined by solving the following boundary integral equation based on Green's second identity (Brebbia and Walker, 1980; Anderson, 1984):

$$\alpha(p)\phi(p) = \int_{\Gamma}\left(\phi(q)\frac{\partial G(q,p)}{\partial \boldsymbol{n}}\right)\mathrm{d}\Gamma - \int_{\Gamma}\left(G(q,p)\frac{\partial \phi(p)}{\partial \boldsymbol{n}}\right)\mathrm{d}\Gamma, \quad p \in \Gamma \tag{1}$$

where Γ represents the entire computational boundary; p and q are the source point (x_0, z_0) and field point (x, z), respectively; α is the solid angle; and G is the Green function considering an image of the Rankine source about the sea floor, and can be written as $G(p, q) = \ln r + \ln r_1$, where $r = \sqrt{(x-x_0)^2 + (z-z_0)^2}$ and $r_1 = \sqrt{(x-x_0)^2 + (z+z_0)^2}$.

On the instantaneous free surface Γ_f, the fully nonlinear kinematic and dynamic boundary conditions are satisfied. The so-called mixed Eulerian-Lagrangian method is used to describe a time-varying free surface. Towards the end of the computational domain, an artificial damping

beach is applied to the free surface so that the wave energy is gradually dissipated in the direction of wave propagation. The profile and magnitude of artificial damping must minimize possible wave reflection at the leading edge of the damping zone while maximizing wave energy dissipation in the damping zone. In the present study, both ϕ- and η-type damping terms are introduced in the free surface boundary conditions, which can be expressed in the Lagrangian expression as follows:

$$\left.\begin{aligned} \frac{\mathrm{D}x}{Dt} &= \frac{\partial \phi}{\partial x} + \mathrm{u}_0 - \mu(x)(x - x_0) \\ \frac{\mathrm{D}\eta}{Dt} &= \frac{\partial \phi}{\partial z} - \mu(x)\eta \\ \frac{\mathrm{D}\phi}{Dt} &= -g\eta + \frac{1}{2}|\nabla\phi|^2 - \frac{p}{\rho} - \mu(x)\phi \end{aligned}\right\} \text{ on } \Gamma_{\mathrm{f}} \qquad (2)$$

where g is the acceleration due to the gravity; p is the pressure; η is the instantaneous free surface elevation; D/Dt is the material derivative; and x_0 is the starting position of the damping layer. The damping coefficient function $\mu(x)$ is defined as

$$\mu(x) = \omega_{\min}\left(\frac{x - x_0}{L_{\mathrm{b}}}\right)^2 \quad \text{for } x_0 \le x \le x_0 + L \qquad (3)$$

where $\omega_{\min}$ denotes the minimum angular frequency of the wave components; and L_{b} is the length of the damping layer and set as $1.5\lambda_{\max}$ (where $\lambda_{\max}$ denotes the maximum wave length of all wave components) in the present study.

In order to consider the pressure of wind, following work by Kharif et al. (2008) and Touboul et al. (2006), the pressure on the interface $z = \eta(x, t)$ is related to the local wave slope. In the present study, a threshold for the local wave slope η_{x} is introduced, above which an energy transfer from wind to wave occurs. The critical value of the slope η_{xc} is set at 0.35 (Touboul et al., 2006) and the pressure can be calculated by the following expression:

$$\begin{cases} p(x) = 0 & \text{if } \eta_{x_{\max}} < \eta_{x_{\mathrm{c}}} \\ p(x) = \rho_{\mathrm{a}} s(\mathrm{u} - c)^2 \dfrac{\partial \eta}{\partial x}(x) & \text{if } \eta_{x_{\max}} \ge \eta_{x_{\mathrm{c}}} \end{cases} \qquad (4)$$

where the constant s is the sheltering coefficient with a value of 0.5 based on experimental data, u is the wind speed, η_{xmax} is the maximum local wave slope, c is the wave phase velocity, and ρ_{a} is the atmospheric density. At the outflow boundary Γ_{r}, the rigid and impermeable boundary condition is satisfied as:

$$\frac{\partial \phi}{\partial n} = 0 \quad \text{on } \Gamma_{\mathrm{d}} \text{ and } \Gamma_{\mathrm{r}}. \tag{5}$$

At the inflow boundary Γ_{i}, fluid motion is generated by a piston wave maker, and for the focused wave the displacement S and velocity u_{p} of the wave maker can be specified as (Ning et al., 2015):

$$\left.\begin{aligned} S &= \sum_{i=1}^{N} \frac{a_i}{T_{\mathrm{r}}} \sin(k_i x_{\mathrm{p}} + \omega_i (t - t_{\mathrm{p}})) \\ u_{\mathrm{p}} &= \sum_{i=1}^{N} \frac{a_i}{T_{\mathrm{r}}} \omega_i \cos(k_i x_{\mathrm{p}} + \omega_i (t - t_{\mathrm{p}})) \end{aligned}\right\} \text{on } \Gamma_{\mathrm{i}} \tag{6}$$

where N is the number of wave components, a_i, k_i, and ω_i are the respective linear wave amplitude, wave number, and angular frequency of the ith component satisfying the linear Doppler-shifted dispersion relationship $(\omega_i - k_i u_0)^2 = g k_i \tanh k_i h$. x_{p} and t_{p} denote the focal position and focal time as predicted by linear wave theory. $T_{\mathrm{r}} = 4\sinh^2(k_i h)/[2k_i h + \sinh(2k_i h)]$ is the transfer function for the piston wave maker and h is the static water depth.

As the above boundary value problem is solved in the time domain, the initial water surface conditions were applied in this study:

$$\phi(x, z, 0) = \eta(x, 0) = 0 \tag{7}$$

In addition, the wave maker properties on the inflow boundary Γ_{i} were imposed gradually using a ramping function, which satisfies calm water conditions and smoothly approaches unity as the simulation proceeds. The ramping function is given by:

$$R_{\mathrm{m}} = \begin{cases} \frac{1}{2}(1 - \cos(\frac{\pi t}{T_{\mathrm{m}}})) & \text{if } t \le T_{\mathrm{m}} \\ 1 & \text{if } t > T_{\mathrm{m}} \end{cases} \tag{8}$$

where T_{m} is specified as the length of time for which the input wave is ramped, here chosen as twice the maximum wave period (i.e., $2T_{\max}$) among all the wave components in the focused wave group.

In this study, the boundary surface was discretized by three-node isoparametric elements, by which Eq. 错误!未找到引用源。 in the discretized form can be expressed as follows:

$$\alpha(p)\phi(p) = -\sum_{j=1}^{\mathrm{M}} \left(\int_{-1}^{1} \frac{\partial G(p, q(\xi))}{\partial n} \phi(q(\xi)) - \frac{\partial \phi(q(\xi))}{\partial n} G(p, q(\xi)) \right) \left| \mathrm{J}(\xi) \right| d(\xi) \quad , \tag{9}$$

where ξ represents the local intrinsic coordinates, M is the number of discretized elements on the surface, and $J(\xi)$ is the Jacobian matrix relating the physical coordinates to the local intrinsic

coordinates within an element. Eventually, the discretized integral equation is transformed into a system of linear algebraic equations.

After solving the boundary value problem and obtaining fluid velocities and the normal vector on the free surface, the free surface boundary conditions in Eq. (2) were advanced in time as described by Ning and Teng (2007). For this purpose, a fourth-order Runge-Kutta (RK4) scheme was adopted. The fluid domain was remeshed at each time step to prevent free-surface nodes from piling up at certain positions. Based on the horizontal coordinates of new nodes obtained through mesh generation, the vertical position and potential could be interpolated using the quadratic shape equation. To find which old line element the new node belongs to, the following criterion was used:

$$\left| L_0 - \sum_{i=1}^{M_1} L_i \right| \to 0.0 \quad , \tag{10}$$

where L_0 is the length of the old line element, L_i is the length of a sub-element consisting of one node in the old element and the new node being considered, and M_1 is the number of sub-elements surrounding the node: here $M_1 = 2$.

3 Validation tests

In order to validate the present model, numerical results were compared with the experimental data in Kharif et al (2008) for the case of a 2D extreme wave under wind action. The wind speed was set as $U = 0$. The tank was 40m in length and 2.6m in height, with a water depth of 1m. The extreme wave was generated by a wavemaker with motion defined by a sine function. The frequency of the sine function varied linearly from the maximum frequency (f_{max} = 1.85Hz) to the minimum frequency (f_{min} = 0.8Hz) over a duration of T = 23.5s. The motion of the wavemaker was governed by:

$$S(\tau) = \begin{cases} \dfrac{a}{F} \cos\left[\displaystyle\int_0^{\tau} \omega(\tau) d\tau \right] & \tau \le T \\ 0 & else \end{cases} \quad , \tag{11}$$

where a is the expected wave amplitude, which is given as 0.007, and F is the transfer function for the wavemaker (Ma, 2007), written as:

$$F = \frac{2\left[\cosh(2kd) - 1\right]}{\sinh(2kd) + 2kd} \quad . \tag{12}$$

Fig. 2 displays the wave elevation at x = 1m in the physical experiment and numerical simulation. There was generally good agreement and the discrepancy during the initial period was due to the use of different ramping functions. Fig. 3 shows the surface elevation at several positions, measured experimentally and computed numerically. The phases and amplitudes of the numerical and experimental wave trains were in good agreement, demonstrating the efficiency of the present numerical method in correctly reproducing the nonlinear evolution of wave groups during the focusing-defocusing cycle.

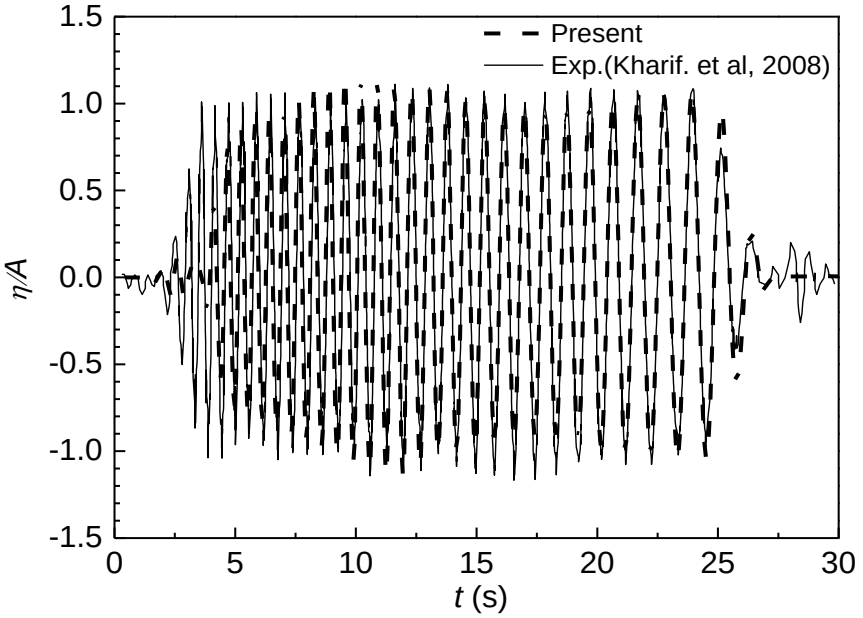

Fig. 2. Surface elevation as a function of time at x = 1m

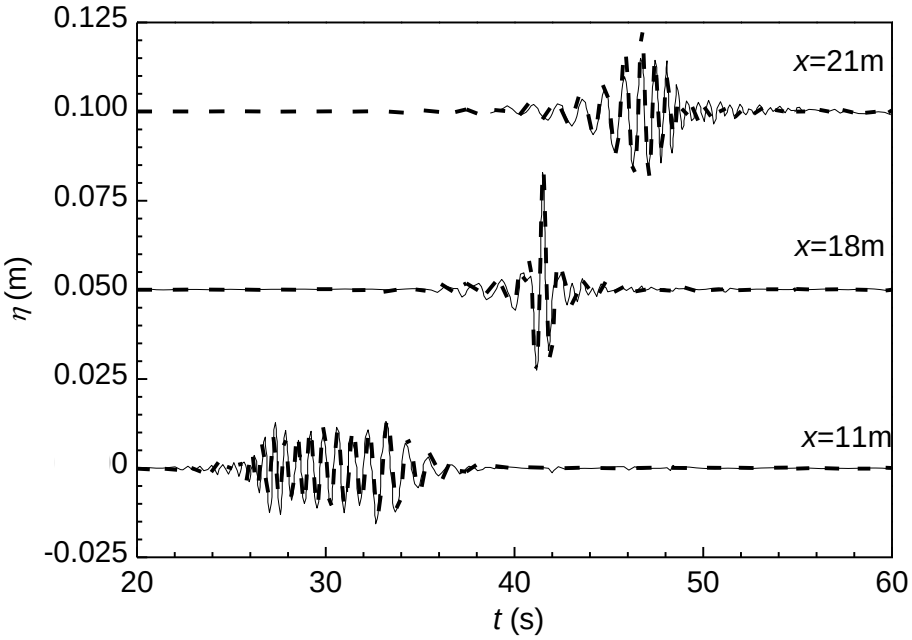

Fig. 3. Surface elevation as a function of time at x = 21, 18, and 11m: experimental (solid line) and numerical simulation (dashed line).

4 The numerical results and discussion

Numerical simulations were next carried out for the focused wave group interaction with wind and wind-driven currents. The effects of the wind velocity, the wave spectra bandwidth, and the input wave group amplitude were studied.

4.1 Evolution of wave groups under wind forcing

The parameters for this case included static water depth h = 0.4m, wave period 0.8s ≤ T ≤ 1.2s (defined as the narrow-band case), 0.6s ≤ T ≤ 1.4s (defined as the wide-band case), and total input group amplitude A_t = 0.05m and A_t = 0.06m. In addition, the wave amplitude was kept constant among the total of 29 wave components, and the desired focusing event occurred at $x_p = 6.5\lambda_{min}$ and $t_p = 16.5T_{min}$ (λ_{min} and T_{min} denote the shortest wavelength and smallest wave period among all wave components, respectively). For the purpose of easier comparison, in the following figures both the focal position and focal time were shifted to 0 on the axes by subtracting the corresponding coordinates with x_p and t_p.

Figure 4 shows the maximum focusing wave amplitude under different wind speed conditions with both the wide- and narrow-bandwidth spectra. The wave amplitude was non-dimensionalized by A_t, which increased as the wind speed increased due to the fact that more energy is transferred to the wave group. In addition, the wave speed seemed to have a greater influence on larger waves: the increase in the wave amplitude for larger waves was more significant with the increase in the wind speed. Frequency bandwidth was also an important factor that affected the extreme wave characteristics. In the case of the narrow-bandwidth spectrum, the wave amplitude grew at the same wind speed, exhibiting stronger nonlinearity.

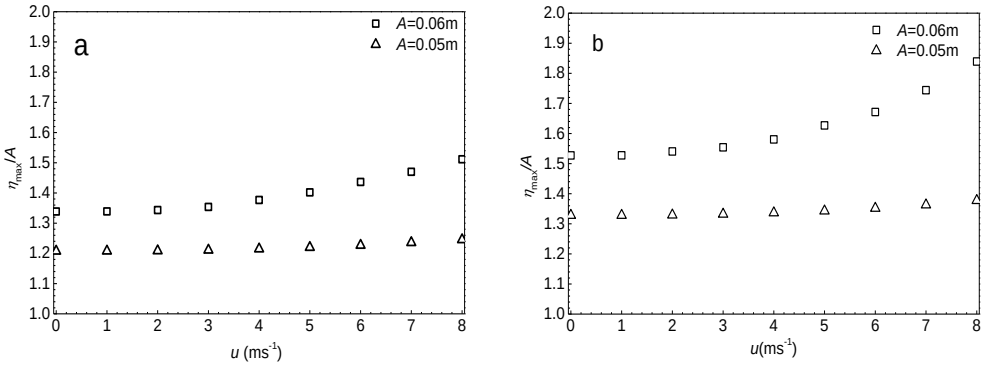

Fig. 4. Plots of focal crest elevation against wind speed at different wave amplitudes and spectra. a. 0.6s≤T≤1.4s and b. 0.8s≤T≤1.2s.

Figure 5 shows the surface elevation when the focusing event occurred at wind speeds of 0, 2, 4, 6, and 8m/s at A_t = 0.06m. The maximum focusing amplitude clearly increased with the increase in the wind speed. This figure also shows the effect of wind by shifting the focal position downstream, most obviously for the narrow-band case. For example, in Fig. 5a the focal position shifted 0.55m downstream at u = 8m/s, while at the same speed the shift in focal position increased to 1.34m for the narrow-band case, as seen in Fig. 5b.

Figure 6. shows the deviation in focal position as a function of the wind velocity. Where A_t = 0.05m, the shift of the focal position did not appear to be sensitive to the wind speed and hardly changed as the wind speed increased, while where A_t = 0.06m, the wind caused a weak downstream shift at the focal point. The same phenomenon was also observed in studies by Kharif et al. (2008) and Touboul et al. (2006), which was due to currents being induced by the wind. The

Jeffreys' sheltering mechanism describes air flow separation over waves. This mechanism is not remarkable for milder waves. However, for steep waves it is well known that the air flow separation results in a much higher energy transfer from wind to waves (Touboul et al., 2008).

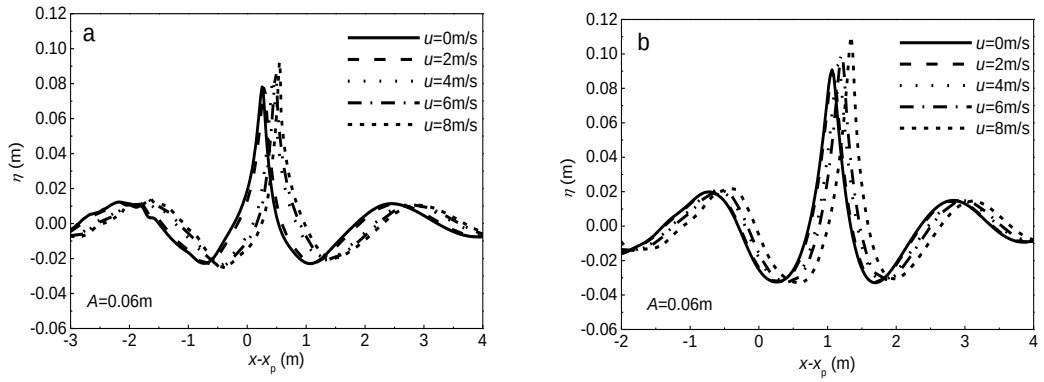

Fig. 5. Spatial distribution of wave elevation at focal time with wind velocities of 0, 2, 4, 6, and 8m/s. a. 0.6s≤*T*≤1.4s and b. 0.8s≤*T*≤1.2s.

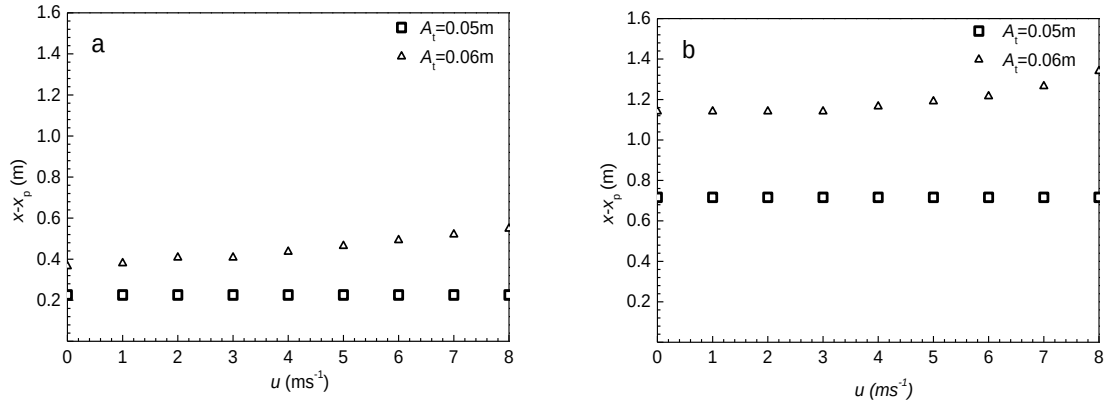

Fig. 6. Plot of focal position deviation against wind speed at different wave amplitudes and spectra.

a. 0.6s≤*T*≤1.4s and b. 0.8s≤*T*≤1.2s.

Figure 7 shows the amplification factor H_{max}/A, as a function of space for the wave group under four different wind forcing conditions (u = 0, 2, 4, and 6m/s). Here H_{max} is the maximum height between the consecutive crest and trough in the transient group. In contrast with the case without wind, there was an asymmetric profile that appeared between the focusing and defocusing stages.

Particularly during the defocusing stage, it was observed that H_{max}/A increased markedly with the increase in the wind speed for the narrow-band case. In Fig. 7a, when u=6m/s the maximum H_{max}/A was around 1.93, but in Fig. 7d the maximum H_{max}/A reached 2.62 at the same wind speed.

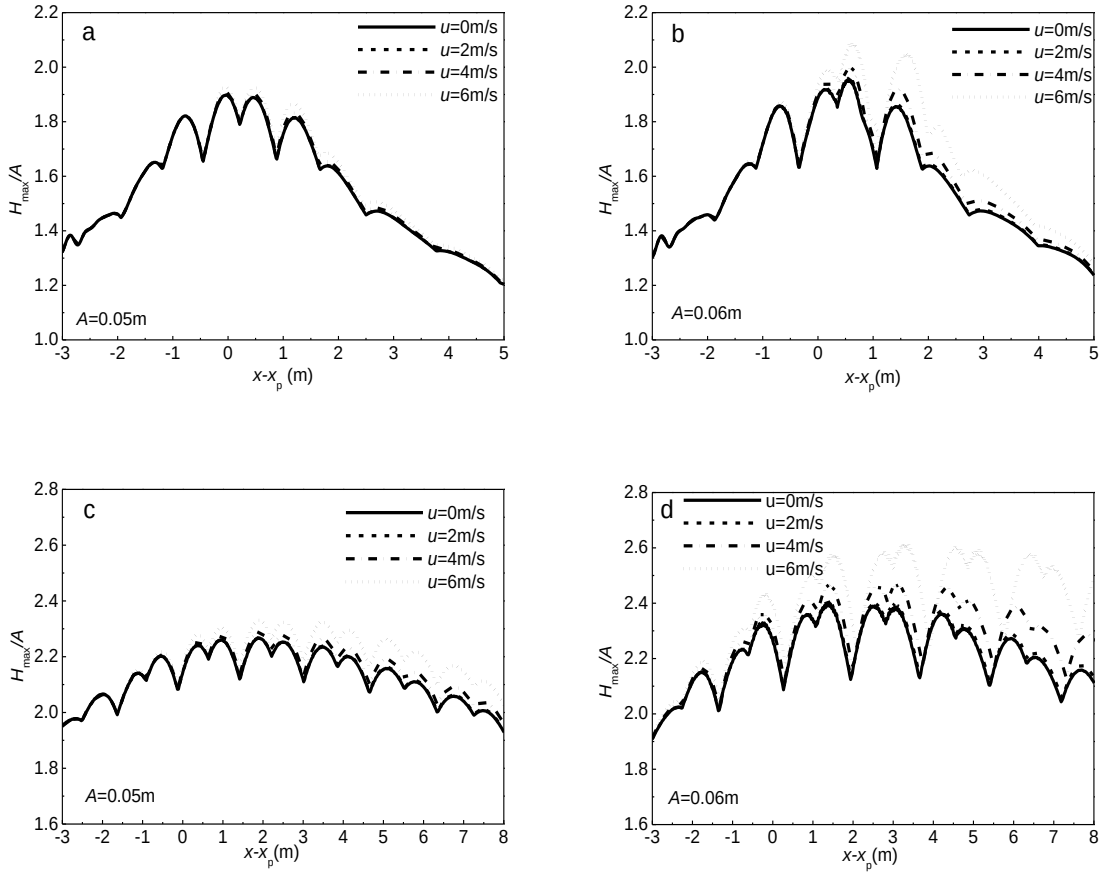

Fig. 7. Evolution of H_{max}/A as a function of space for various wind speeds at different wave amplitudes and spectra.

a. 0.6s≤T≤1.4s , b. 0.6s≤T≤1.4s, c. 0.8s≤T≤1.2s and d. 0.8s≤T≤1.2s.

The spectral energy evolution for wave focusing and defocusing is shown for cases with and without wind action in Fig. 8. An input group amplitude of A = 0.06m was considered for both the narrow-band and wide-band cases. Five representative spatial points, including upstream points, the actual focal point x_f, and downstream points are plotted. The solid line indicates the density spectrum at the first upstream reference point, and the dashed lines denote those at the other marked points in the figures. As the wave group approached the focal position, the transfer of

spectral energy from the primary frequency to higher frequencies could clearly be seen. The wave energy was then transferred from the high frequencies back to the fundamental one, and the corresponding spectra gradually returned to their original reference values during the wave defocusing process in the case without wind. This means that the nonlinear energy transfer was reversible in the focusing and defocusing processes and the effects of the wave to wave interactions were gradually diminished. In contrast, when the wind velocity *u* was 6m/s, the energy transferred to the high frequencies could not recover to its initial reference level as shown in Fig. 8. Energy transfer to the high frequencies was still visible at the focal point.

4.2 Wind-driven currents

The presence of wind forcing introduces a thin surface drift layer, which may have important effects on the evolution of the wave groups (Banner and Phillips, 1974). This layer has high vorticity and the velocity profile depends strongly on the water depth (Phillips and Banner, 1974); however, for simplicity, the layer can be modeled as a uniform surface current (Kharif et al., 2008) with a magnitude that is typically a few percent of the wind speed. Figure 9 compares the distribution of the focused crest elevation under wind action with and without wind-driven currents, with linear wind speed predictions of *u*=2 and 4m/s. It shows that, as the wave amplitude increases, the maximum wave elevation increases and deviates from the linear solution. Furthermore, the maximum crest elevation increased more rapidly for the case with wind only, but less significantly for the case with the wind-driven currents due to a decreasing wave nonlinearity.

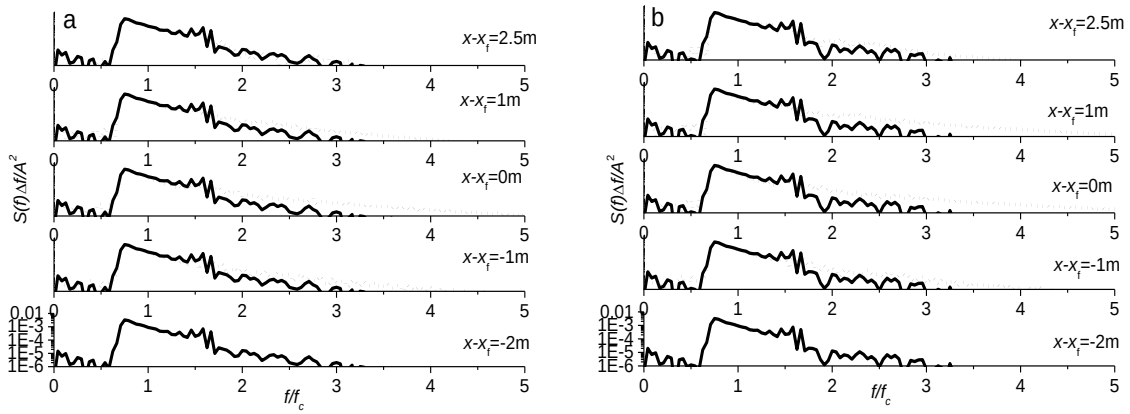

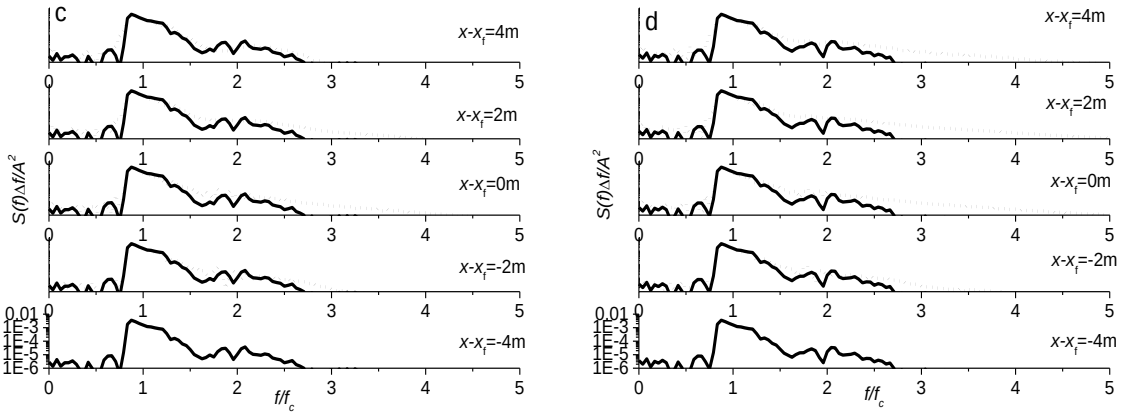

Fig. 8. Energy spectrum at different points for cases with and without wind.

a. 0.6s≤*T*≤1.4s, *u*=0m/s; b. 0.6s≤*T*≤1.4s, *u*=6m/s; c. 0.8s≤*T*≤1.2s, *u*=0m/s; and d. 0.8s≤*T*≤1.2s, *u*=6m/s.

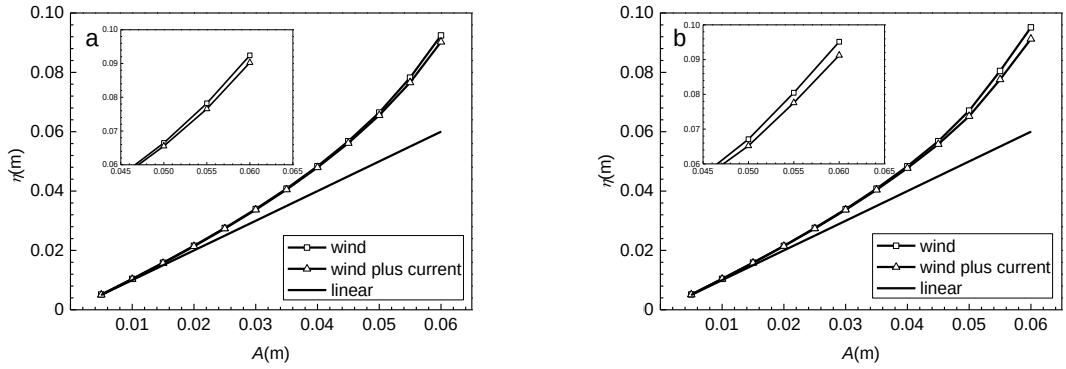

Fig. 9. Comparison of focus wave amplitude under the action of various sources at *u*=2m/s and 4m/s. a. *u*=2m/s and b. *u*=4m/s.

Figure 10 and 11 show the temporal history of the wave elevation at the focusing position and the spatial distribution of the wave elevation at the focusing time for four different cases, i.e., pure wave (*u*=0m/s, u_0=0m/s), wind action (*u*=6m/s, u_0=0m/s), and the dual action of winds and induced currents (*u*=6m/s, u_0=0.054m/s). It can be seen that the focusing time delays and the focusing position shifted downstream compared with those in the pure waves for two cases (wind only and wind-driven currents). In particular, the postponement of the focal time and the focal position was most significant for the wind-driven currents case, because both the influence of the wind and the

wind-driven currents were taken into account. On the other hand, due to the nonlinear effect, the delays in the focal position and the focal time were more obvious in the narrow-band spectrum. For example, in Fig. 10d the delay in focal time for the case of u=6m/s, u_0=0.054m/s was 2.9s, while in Fig. 11d the delay in focal position for the same case was 4.14m.

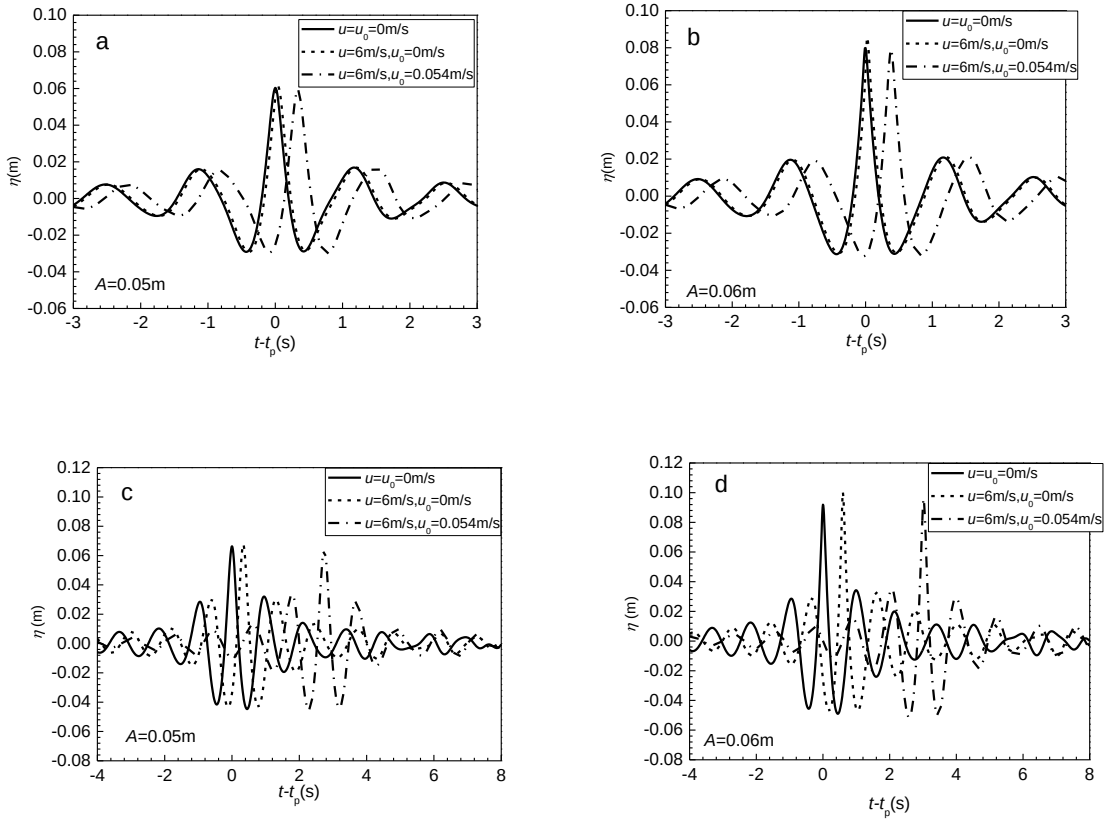

Fig. 10. Comparison of time history at focal position.

a. 0.6s≤T≤1.4s, b. 0.6s≤T≤1.4s, c. 0.8s≤T≤1.2s and d. 0.8s≤T≤1.2s.

5 Conclusions

The influence of wind on the characteristics of the extreme waves was investigated using a fully nonlinear wind and wave mixing 2-D numerical tank model. The wind-excited pressure was modelled using a modified Jeffreys' sheltering mechanism model. Through a series of numerical investigations, effects of the wind pressure on the extreme wave were described and can be classified as follows. First, the maximum focusing amplitude of the extreme wave was increased due to the presence of a wind pressure. Second, the current induced by the wind weakly shifted the

focusing position of the extreme waves. The cases with narrow-band spectra and larger input wave amplitudes were more significantly influenced by wind. Thirdly, unlike the cases with no wind, the wave profiles for cases with wind were asymmetric between the focusing and defocusing stages. During the process of defocusing in particular, a clear increase in H_{max}/A was observed as the wind speed increased, for the narrow-band case. Finally, the wind affected the spectral evolution of the focusing wave groups. For the case without wind, as the wave group approached the focusing position, there was a clear transfer of spectral energy from the primary frequency to higher frequencies. Then there was a reverse transfer of the wave energy and the corresponding spectra gradually recovered to their original reference values during the wave defocusing process. In contrast, considering when the wind velocity is 6m/s, the energy transferred to the higher frequencies was not able to return to the initial reference level. The direct comparison of the effects of wind, currents, and wind-driven currents reveals that the maximum crest elevation increases more clearly in the case of wind only, and least of all in the case with currents only. In addition, because the influence of both winds and currents was taken into account in the wind-driven currents case, the focusing time and the focusing position were most obviously delayed. It must be noted that the present study is based on the nonlinear potential-flow theory. For more detail on the interactions of wind and waves, viscous effects should be considered in the future investigations.

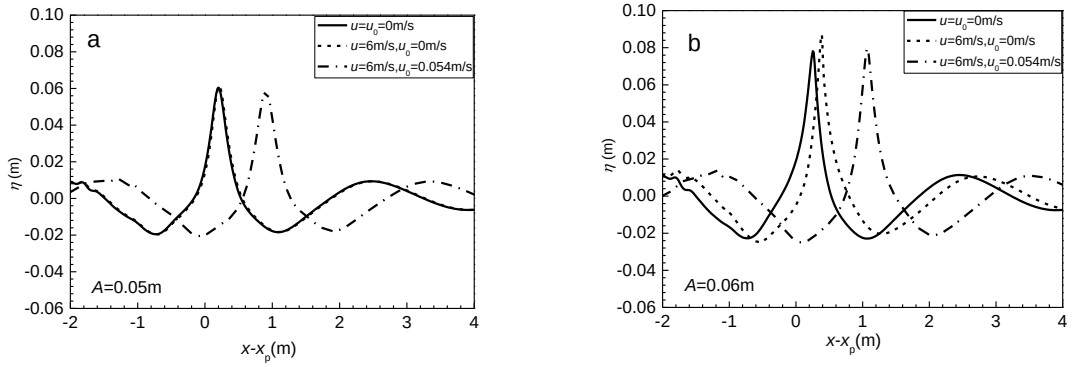

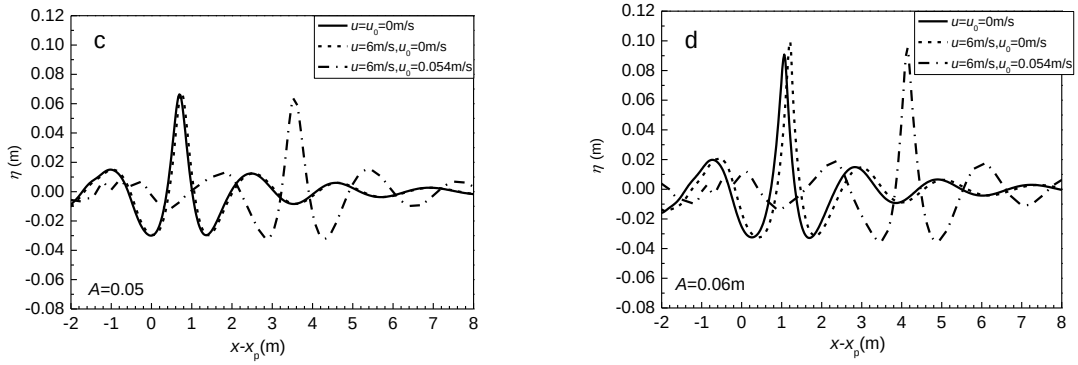

Fig. 11. Comparison of spatial distribution at different focal times

a. 0.6s≤T≤1.4s, b. 0.6s≤T≤1.4s, c. 0.8s≤T≤1.2s and d. 0.8s≤T≤1.2s

References

Anderson M P. 1984. The boundary integral equation method for porous media flow. Eos Transactions American Geophysical Union, 65(9), 76–76

Baldock T E, Swan C, Taylor P H. 1996. A laboratory study of nonlinear surface waves on water. Philosophical Transactions of the Royal Society of London A: Mathematical, Physical and Engineering Sciences, 354(1707): 649–676

Banner M L, Phillips O M. 1974. On the incipient breaking of small scale waves. Journal of Fluid Mechanics, 65(4): 647–656

Benjamin T B, Feir J E. 1967. The disintegration of wave trains on deep water: Part 1. Theory. Journal of Fluid Mechanics, 27(3): 417–430

Brandini C, Grilli S. 2001. Modeling of freak wave generation in a 3D-NWT. 11th International Offshore and Polar Engineering Conference, 17-22 June, Stavanger, Norway

Brebbia C A, Walker S. 1980. Boundary Element Techniques in Engineering. Amsterdam: Elsevier

Ducrozet G, Bonnefoy F, Ferrant P. 2008. Analysis of freak waves formation with large scale fully nonlinear high order spectral simulations. 18th International Offshore and Polar Engineering Conference, July 6-11, Vancouver, BC, Canada

Fuhrman D R, Madsen P A. 2006. Numerical simulation of extreme events from focused directionally spread wave fields. In: Proceedings of the 30th International Conference on Coastal Engineering. San Diego, California, USA: World Scientific

Fulgosi M, Lakehal D, Banerjee S, et al. 2003. Direct numerical simulation of turbulence in a sheared air-water flow with a deformable interface. Journal of Fluid Mechanics, 482: 319–345

Grue J, Clamond D, Huseby M, et al. 2003. Kinematics of extreme waves in deep water. Applied Ocean Research, 25(6): 355–366

Hu Jinpeng, Zhang Yunqiu. 2014. Analysis of energy characteristics in the process of freak wave generation. China Ocean Engineering, 28(2): 193–205

Johannessen T B, Swan C. 2001. A laboratory study of the focusing of transient and directionally spread surface water waves. Proceedings of the Royal Society A: Mathematical, Physical and Engineering Sciences, 457(2008): 971–1006

Kharif C, Giovanangeli J P, Touboul J, et al. 2008. Influence of wind on extreme wave events: experimental and numerical approaches. Journal of Fluid Mechanics, 594: 209–247

Kharif C, Pelinovsky E, Talipova T, et al. 2001. Focusing of nonlinear wave groups in deep water. Journal of Experimental and Theoretical Physics Letters, 73(4): 170–175

Liu P C, MacHuchon K R, Wu C H. 2004. Exploring rogue waves from observations in South Indian Ocean. Actes de colloques – IFREMER, 39: 1-10.

Longuet-Higgins M S. 1952. On the statistical distributions of sea waves. Journal of Marine Research, 11(3): 245–265

Longuet-Higgins M S. 1980. On the distribution of the heights of sea waves: some effects of nonlinearity and finite band width. Journal of Geophysical Research: Oceans, 85(C3): 1519–1523

Ma Q W. 2007. Numerical generation of freak waves using MLPG_R and QALE-FEM methods. Computer Modeling in Engineering & Sciences, 18(3): 223–234

Mori N, Liu P C, Yasuda T. 2002. Analysis of freak wave measurements in the Sea of Japan. Ocean Engineering, 29(11): 1399–1414

Mori N, Yasuda T. 2002. Effects of high-order nonlinear interactions on unidirectional wave trains. Ocean Engineering, 29(10): 1233–1245

Nakayama A, Sakio K. 2002. Simulation of flows over wavy rough boundaries. Center for Turbulence Research, Annual Research Briefs, Stanford University/NASA Amers Research Center, 2002: 313–324

Ning D Z, Teng B. 2007. Numerical simulation of fully nonlinear irregular wave tank in three

dimension. International Journal for Numerical Methods in Fluids, 53(12): 1847–1862

Ning Dezhi, Zhuo Xiaoling, Hou Tiancong, et al. 2015. Numerical investigation of focused waves on uniform currents. International Journal of Offshore and Polar Engineering, 25(1): 19–25

Onorato M, Osborne A R, Serio M, et al. 2001. Freak waves in random oceanic sea states. Physical Review Letters, 86(25): 5831–5834

Onorato M, Osborne A R, Serio M. 2002. Extreme wave events in directional, random oceanic sea states. Physics of Fluids, 14(4): L25–L28

Osborne A R, Onorato M, Serio M. 2000. The nonlinear dynamics of rogue waves and holes in deep-water gravity wave trains. Physics Letters: A, 275(5 - 6): 386–393

Phillips O M, Banner M L. 1974. Wave breaking in the presence of wind drift and swell. Journal of Fluid Mechanics, 66(4): 625–640

Sullivan P P, Edson J B, McWilliams J C, et al. 2004. Large-eddy simulations and observations of wave-driven boundary layers. 16th Symposium on Boundary Layers and Turbulence. August 8-13, Portland.

Sullivan P P, McWilliams J C. 2002. Turbulent flow over water waves in the presence of stratification. Physics of Fluids, 14(3): 1182–1195

Sullivan P P, McWilliams J C, Moeng C H. 2000. Simulation of turbulent flow over idealized water waves. Journal of Fluid Mechanics, 404: 47–85

Tian Zhigang, Choi W. 2013. Evolution of deep-water waves under wind forcing and wave breaking effects: numerical simulations and experimental assessment. European Journal of Mechanics - B/Fluids, 41: 11–22

Touboul J. 2007. On the influence of wind on extreme wave events. Natural Hazards and Earth System Sciences, 7(1): 123–128

Touboul J, Giovanangeli J P, Kharif C, et al. 2006. Freak waves under the action of wind: experiments and simulations. European Journal of Mechanics - B/Fluids, 25(5): 662–676

Touboul J, Kharif C, Pelinovsky E, et al. 2008. On the interaction of wind and steep gravity wave groups using Miles' and Jeffreys' mechanisms. Nonlinear Processes in Geophysics, 15(6): 1023–1031

Yan S, Ma Q W. 2011. Improved model for air pressure due to wind on 2D freak waves in finite depth. European Journal of Mechanics - B/Fluids, 30(1): 1–11

Zou Qingping, Chen H F. 2016. Numerical simulation of wind effects on the evolution of freak waves. 26th International Ocean and Polar Engineering Conference, June 26 - July 1, Rhodes, Greece.